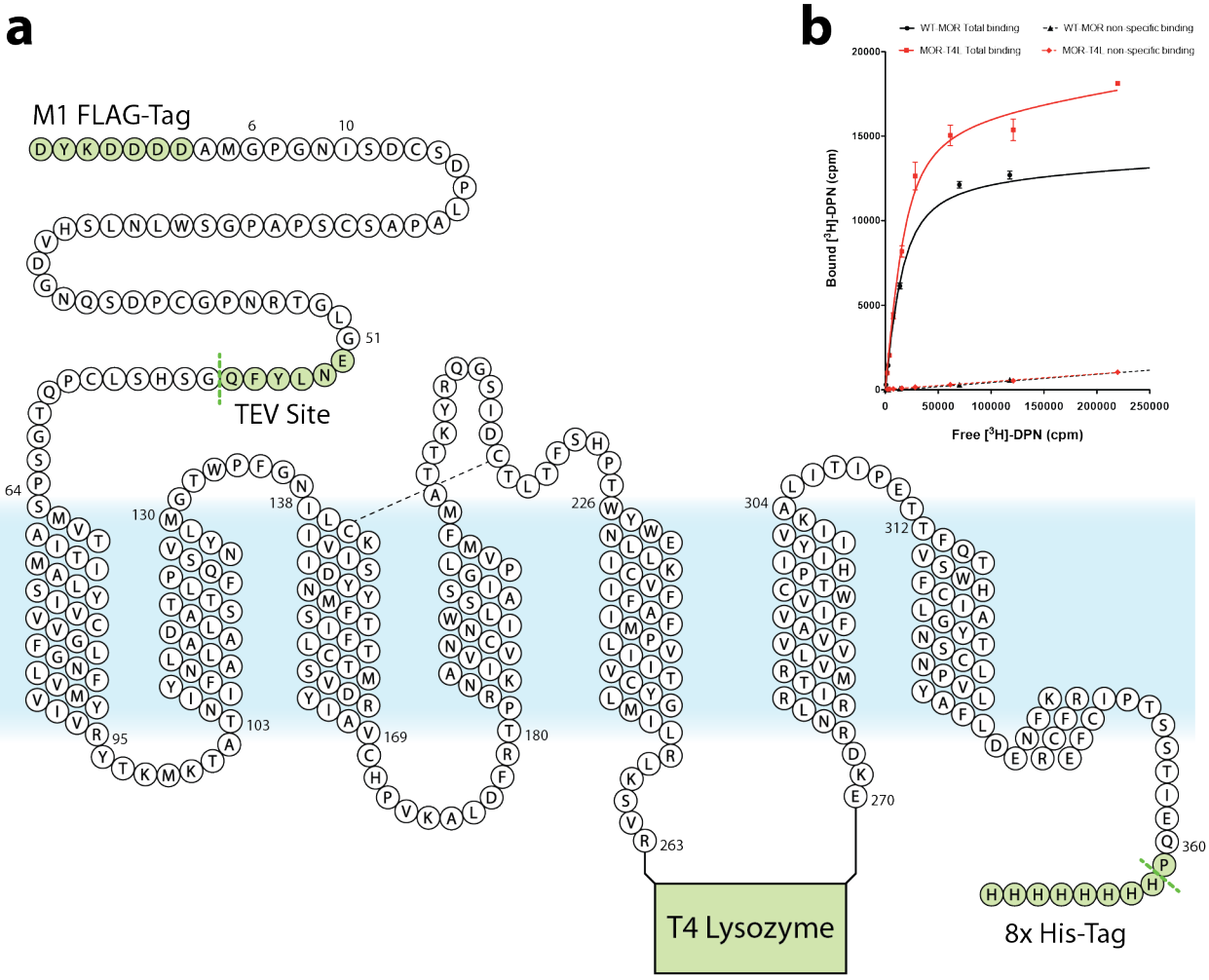

Supplementary Figure 1. μ-Opioid receptor crystallography construct and radioligand binding studies

a. The final crystallization construct (μOR-T4L) is shown here with all modifications made to the *Mus musculus* wild-type μOR. To remove the disordered amino-terminal sequence (residues 6-51) a TEV site was introduced after Gly51. The carboxy-terminal disordered region (residues 361-398) were truncated. To facilitate protein purification, the FLAG affinity sequence was introduced at the N-terminus and an octa-histidine tag was introduced at the C-terminus. A proline was introduced after Q360 to allow efficient removal of the octa-histidine tag with carboxypeptidase A treatment. The third intracellular loop (residues 264-269) was replaced with a cysteine-less T4 lysozyme (T4L).

b. Saturation binding curves of total and non-specific [^{3}H]DPN binding to the wild-type mouse μOR and to μOR-T4L. Curves are representative of two experiments carried out in triplicate (experimental details in online methods). [^{3}H]DPN K_D values are 0.46 ± 0.09 nM and 0.42 ± 0.07 nM for μOR and μOR-T4L, respectively.

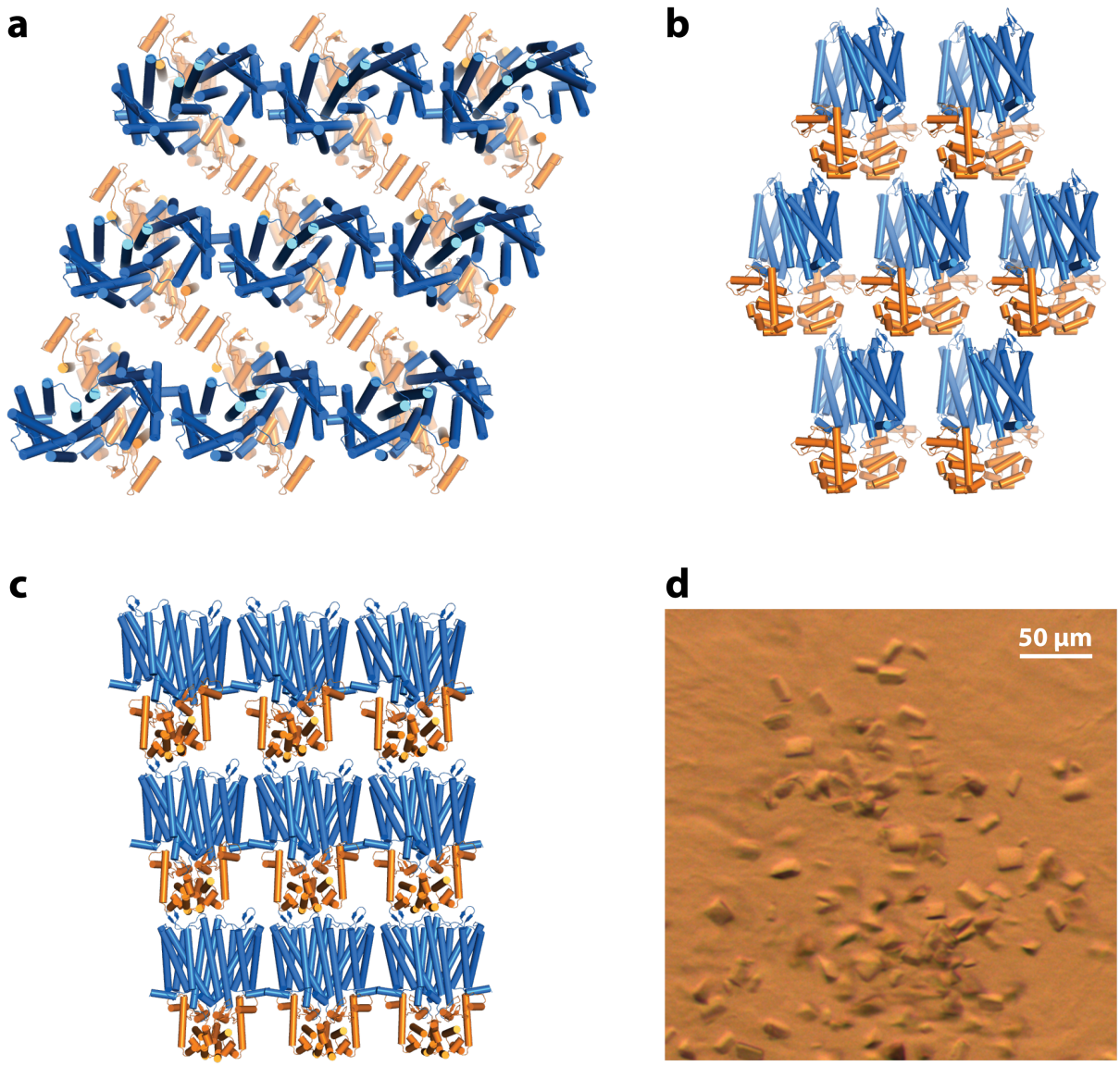

Supplementary Figure 2. µOR-T4L crystals and lattice packing.

a-c. Lattice packing of µOR-T4L crystals with µOR depicted in blue and T4L in orange. As observed for other GPCRs crystallized as T4 lysozyme fusion proteins using the *in meso* method, µOR-T4L packs with alternating aqueous and lipidic layers. **a.** Within the plane of the lipidic layer, µOR makes abundant nonpolar contacts with other µOR molecules mediated by TM5 and TM6. More limited µOR-µOR packing occurs through TM1, TM2 and Helix 8. **b.** Within the aqueous layer, T4L makes contact with other T4L molecules through both the large and small domains. **c.** T4L-receptor contacts are primarily mediated through ECL2 of µOR.

d. Crystals of µOR-T4L under brightfield illumination. Average crystals grew to 20 µm in each dimension before harvesting.

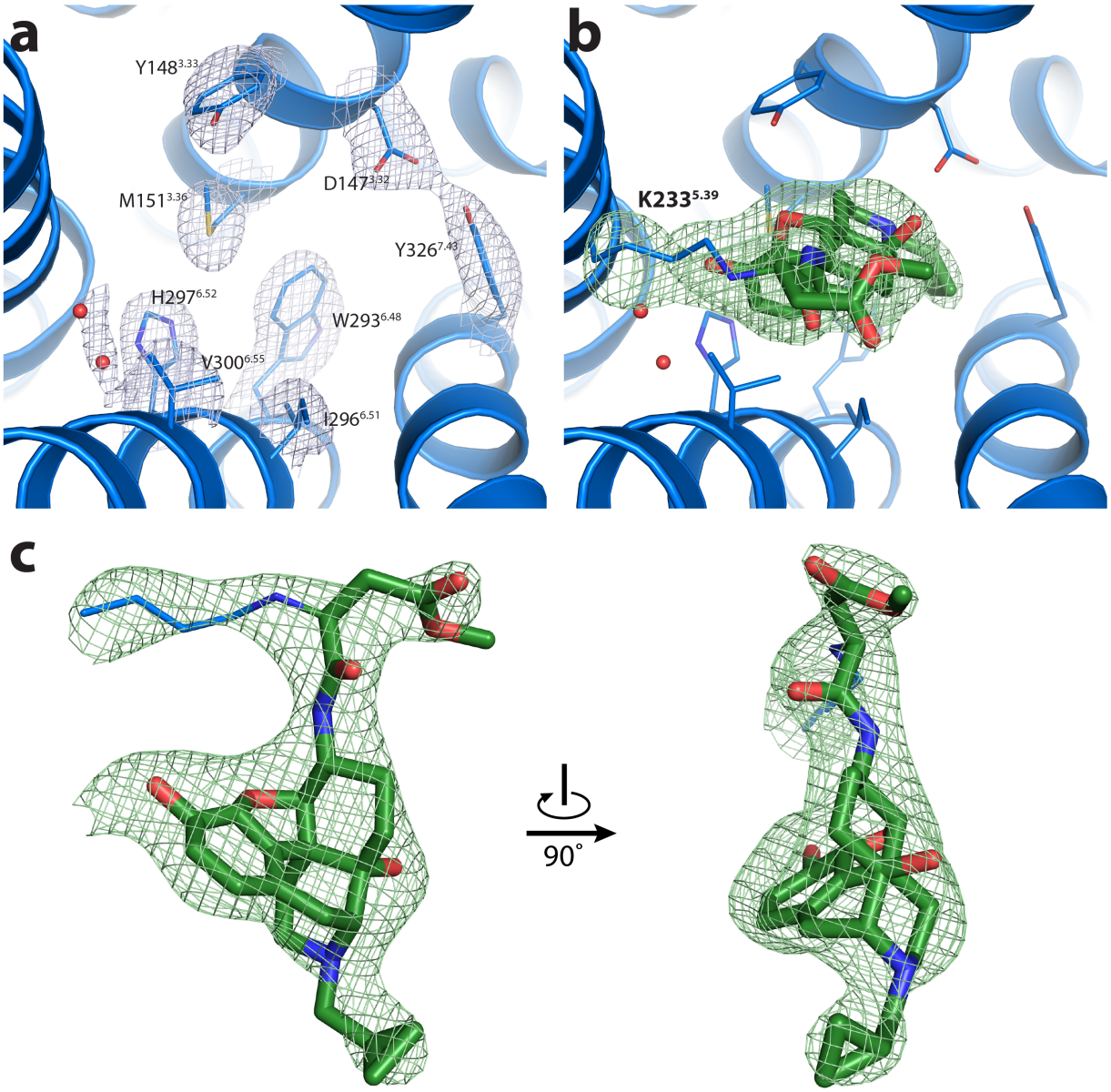

Supplementary Figure 3. Electron density within the ligand-binding pocket.

The ligand β-FNA is bound within a μOR ligand-binding pocket and covalently tethered to K233$^{5.39}$. **a.** Maps for binding pocket residues and for two water molecules are shown with mesh depicting the $2F_o$-F_c electron density contoured at 1.3 σ. **b.** The same view of the binding pocket is shown with an omit map of β-FNA and the K233$^{5.39}$ side chain atoms contoured at 3.0 σ. The electron density supports the previously characterized covalent link between the side chain amine of K233$^{5.39}$ and the highly electrophilic carbon of β-FNA[48]. **c.** Two more views of the electron density around the β-FNA ligand with the covalently tethered K233$^{5.39}$ side chain are shown. The density provides sufficient features to reliably position the cyclopropyl moiety and the core morphinan group. Superscripts indicate Ballesteros-Weinstein numbers.

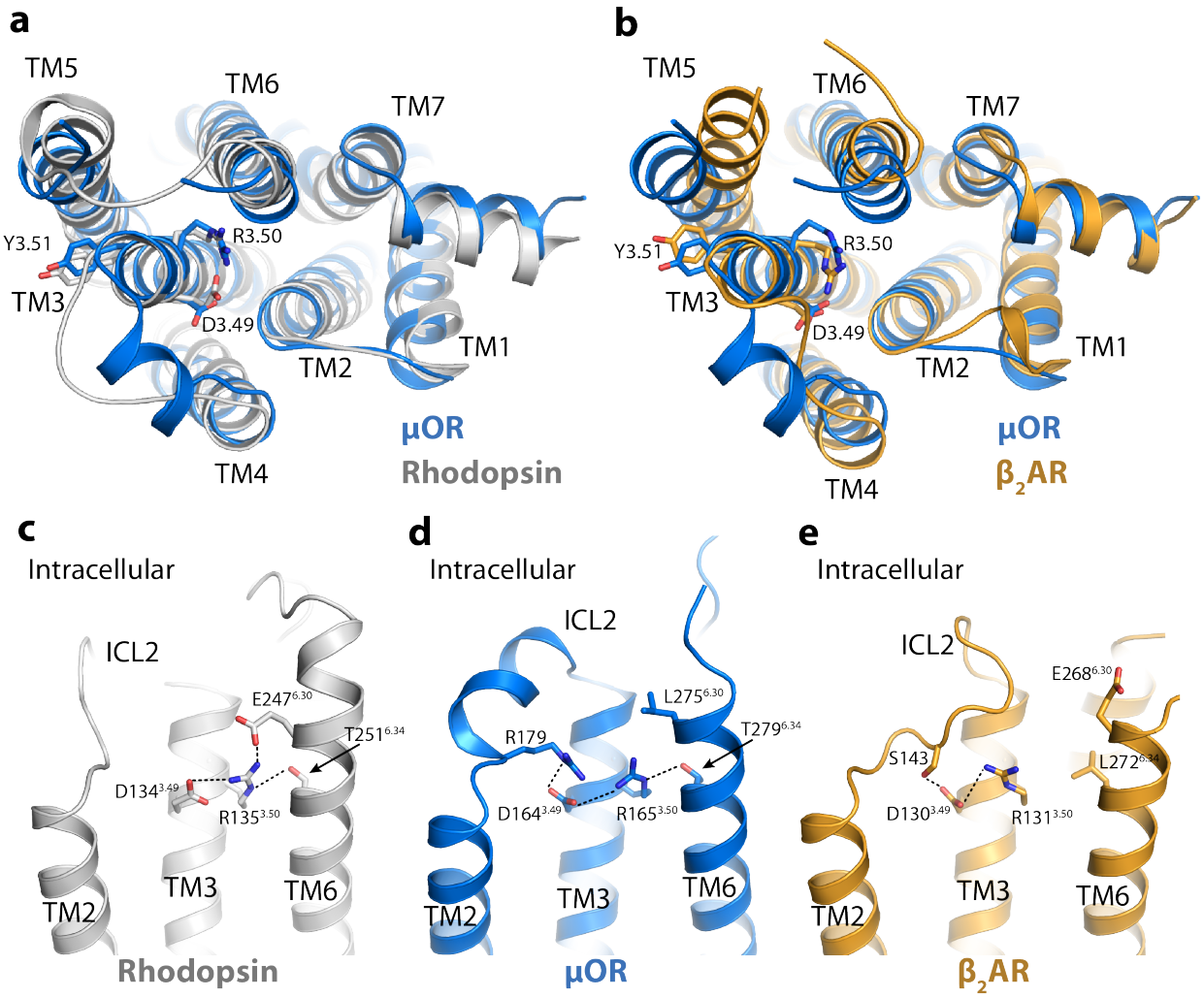

Supplementary Figure 4. Intracellular domain of μOR.

Although the highly conserved residues of the DRY motif in the μOR make similar contacts to those seen in the β_2AR, the relative positions of TM3, TM5, and TM6 are similar to rhodopsin. The intracellular side of μOR more closely resembles rhodopsin (**a**) as compared to β_2AR (**b**). A closer view of the region around the DRY motif is shown for each receptor in **c,d,e**. In rhodopsin, the highly conserved R135$^{3.50}$ residue forms an ionic interaction with D134$^{3.49}$ and E247$^{6.30}$ **c**. In both the μOR and β_2AR, the conserved aspartate and arginine of the DRY motif recruit a polar residue from ICL2 to form an extended bonding network. However, in the μOR, T279$^{6.34}$ engages in a polar interaction with R165$^{3.50}$.

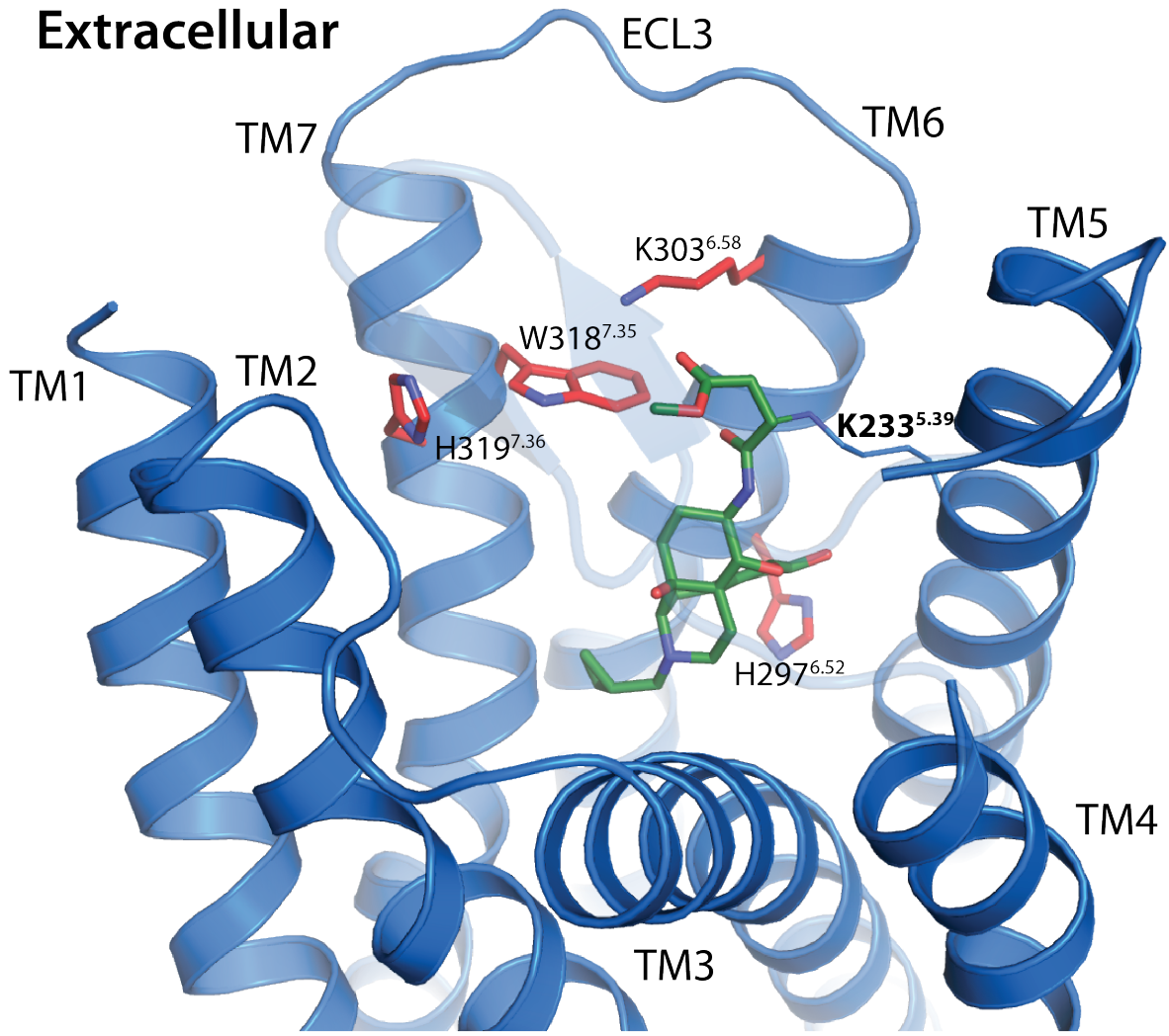

Supplementary Figure 5. Residues critical for DAMGO binding.

The high-affinity, μOR selective peptide DAMGO binds in a pocket that overlaps with β-FNA. Mutation of the residues shown in red severely affects DAMGO binding to μOR. While H297 makes contacts with β-FNA, residues K303, W318, and H319 do not. The binding site for peptides like DAMGO therefore overlaps with morphinan ligands but likely extends further towards the extracellular side of the receptor.

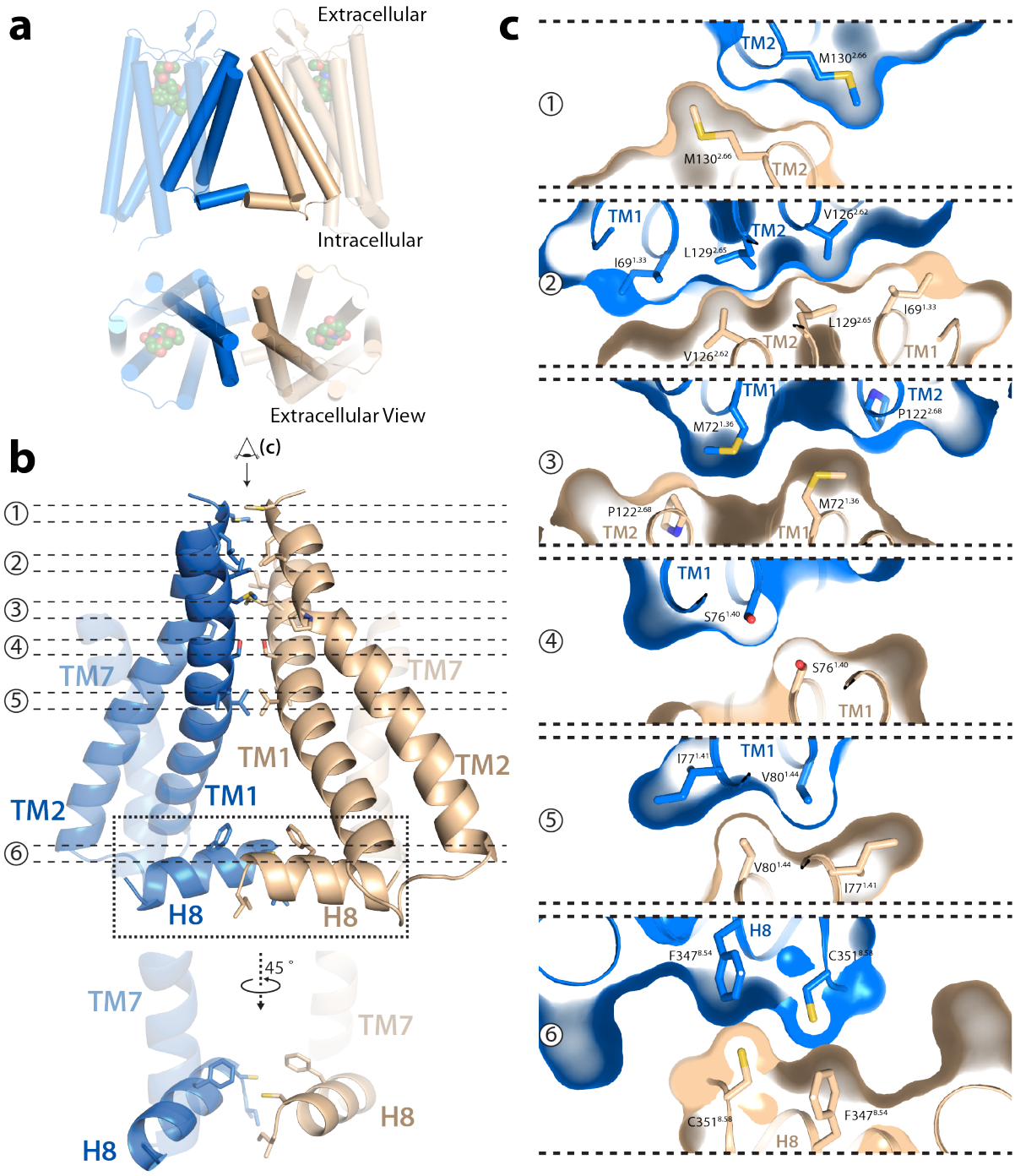

Supplementary Figure 6. Interface TM1-TM2-H8 between two μOR protomers.
Although the larger contact between μOR molecules is observed through the TM5-TM6 interface, a more limited interaction is observed with another crystallographically related μOR molecule involving TMs 1-2 and Helix 8. This interface is described in more detail here. **a,** Side view (top) and extracellular view (bottom) of the TM1-TM2-H8 interface. **b,** The interface is expanded and shown in detail with interacting residues within 4.2 Å shown as sticks. **c**, Tomographic representation along the interface viewed from the extracellular side (as indicated in panel c).

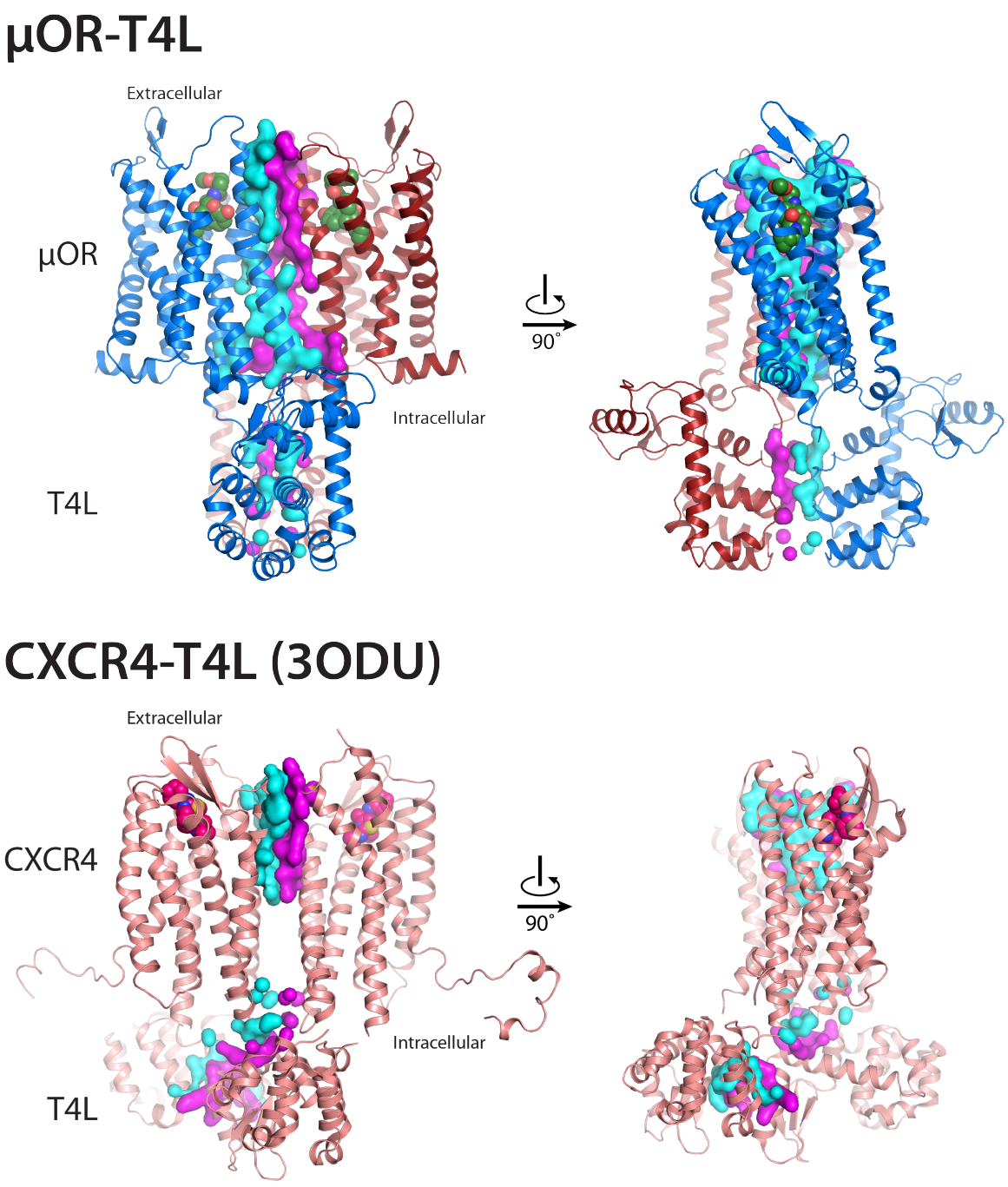

Supplementary Figure 7. Interface between μOR-T4L and CXCR4-T4L pairs.

The interface between two μOR-T4L molecules is shown, with the interface for one subunit depicted in cyan and the other in magenta. Each μOR monomer buries 1492 Å^2 of its partnered monomer, resulting in a total buried surface area of 2984 Å^2 for one μOR- μOR pair. The T4L-T4L contacts within the interface are more limited, with each T4L monomer burying 114 Å^2 of its paired T4L. This is in comparison to a smaller buried surface area for the similar interface observed in the CXCR4-T4L crystal structures. In the structure of CXCR4-T4L depicted here (PDB ID: 3ODU), each receptor buries 784 Å^2 of its partnered monomer while the T4L-T4L

contact amounts to 287 $Å^2$ of buried surface area. Within the available CXCR4 structures, the highest buried surface area across this interface is 1077 $Å^2$ (PDB ID: 3OE0). Buried surface area calculations were performed using the PDBePISA server.

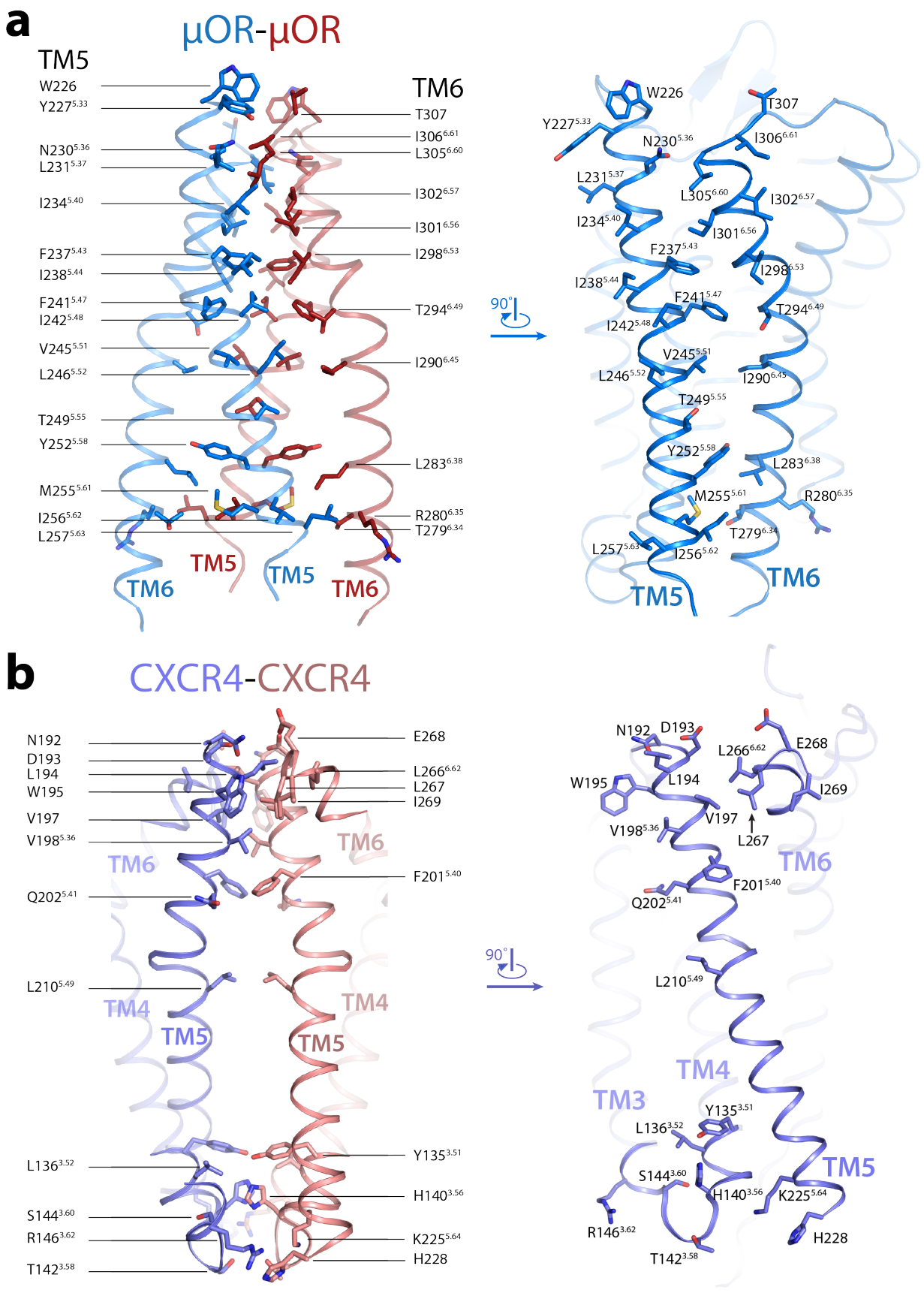
a
μOR-μOR
TM5
TM6
W226
Y227^5.33
N230^5.36
L231^5.37
I234^5.40
F237^5.43
I238^5.44
F241^5.47
I242^5.48
V245^5.51
L246^5.52
T249^5.55
Y252^5.58
M255^5.61
I256^5.62
L257^5.63
T307
I306^6.61
L305^6.60
I302^6.57
I301^6.56
I298^6.53
T294^6.49
I290^6.45
L283^6.38
R280^6.35
T279^6.34
TM5
TM5
TM6
TM6
90°
W226
T307
Y227^5.33
N230^5.36
I306^6.61
L231^5.37
L305^6.60
I302^6.57
I234^5.40
I301^6.56
F237^5.43
I298^6.53
I238^5.44
F241^5.47
T294^6.49
I242^5.48
V245^5.51
L246^5.52
I290^6.45
T249^5.55
Y252^5.58
L283^6.38
M255^5.61
R280^6.35
T279^6.34
L257^5.63
I256^5.62
TM5
TM6
b
CXCR4-CXCR4
N192
D193
L194
W195
V197
V198^5.36
Q202^5.41
L210^5.49
L136^3.52
S144^3.60
R146^3.62
T142^3.58
E268
L266^6.62
L267
I269
F201^5.40
Y135^3.51
H140^3.56
K225^5.64
H228
TM6
TM6
TM4
TM4
TM5
TM5
90°
N192
D193
L266^6.62
E268
W195
L194
I269
V197
V198^5.36
L267
TM6
F201^5.40
Q202^5.41
L210^5.49
TM4
TM3
Y135^3.51
L136^3.52
TM5
S144^3.60
H140^3.56
K225^5.64
R146^3.62
H228
T142^3.58

Supplementary Figure 8. Network of interactions for the TM5-TM6 interface and comparison with CXCR4. a. The four helix bundle interface between TM5-TM6 of two μOR protomers (blue and red). The 28 contacting residues (defined as less than 4.2 Å from each protomer) are shown as sticks. The right panel displays a 90º rotated view of one protomer viewed from the interface. **b,** The dimeric interface observed in the crystal structure of CXCR4 resembles the μOR interface but with a less extensive network of interacting residues. We show 3OE0 here because it has the most extensive interaction network within available CXCR-T4L structures. The CXCR4 dimeric interface is similar to the one observed for the μOR in that the dimeric interactions towards the extracellular side of the receptor are driven by residues in TM5 and TM6. Unlike μOR, the dimeric interface for CXCR4 may also be driven by residues in TM3 and TM4. However, this full complement of interactions is not observed in all of the available CXCR4 structures, perhaps as a result of different arrangements of T4L at the intracellular side of the receptor.

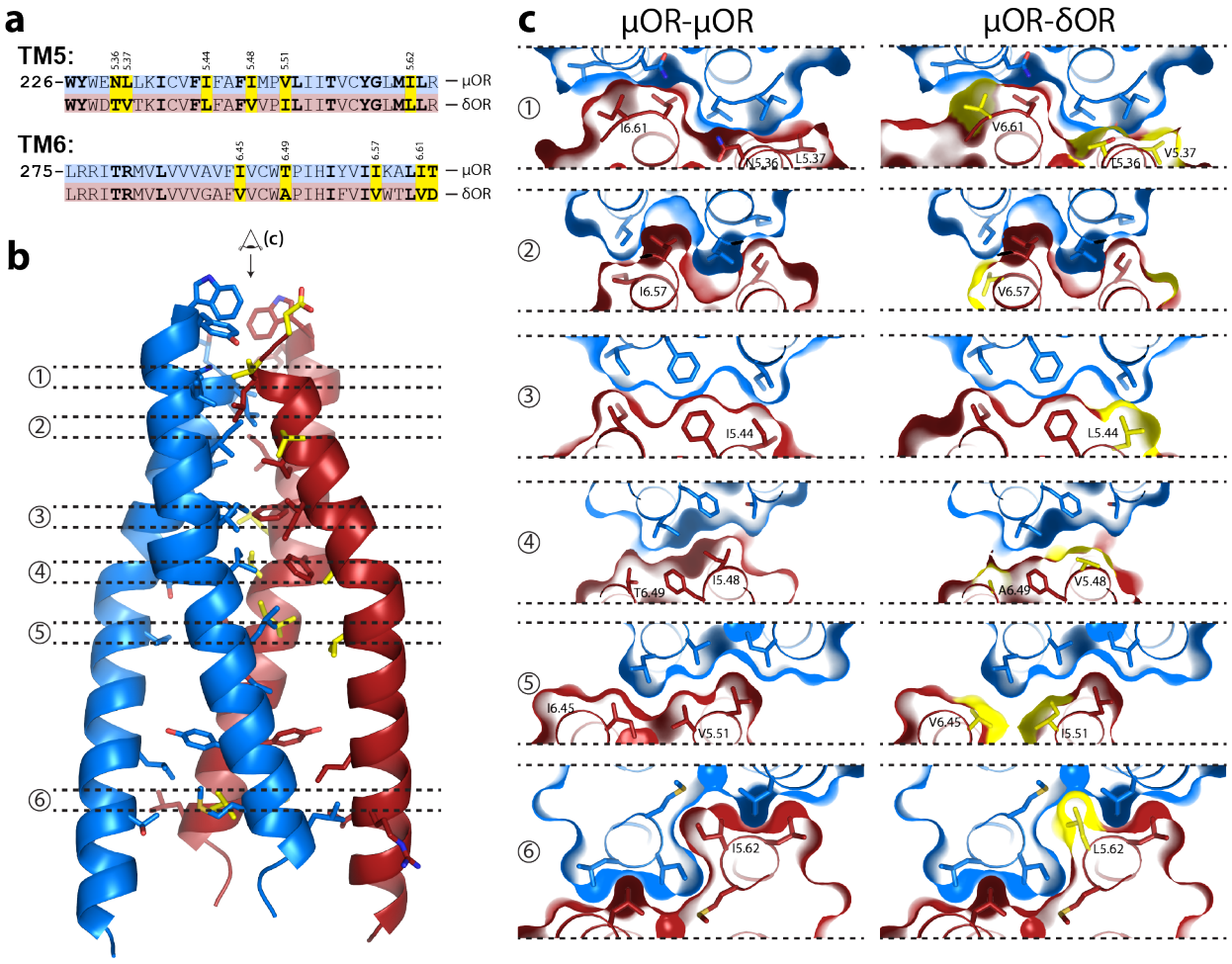

Supplementary Fig. 9: Comparison of the TM5-6 interface between μOR-μOR and μOR-δOR.

a, Alignment of TM5 and TM6 sequences from the μOR and δOR. Interacting residues are shown in bold font, and non-strictly conserved residues are highlighted in yellow. **b**, Potential μOR-δOR four-helix bundle interface shown in detail with TM5-TM6 of μOR in blue and TM5-TM6 of δOR in red. Yellow sticks indicate residues that are different in δOR as compared to μOR. Here, a homology model of δOR based on the μOR was aligned with the red protomer. **c**, Tomographic representation along the interface viewed from the extracellular side (as indicated in panel b). The differences between μOR and δOR results in a slightly different dimeric interface but these changes do not result in severe clashes or considerably unfavorable interactions. Therefore, the differences in the residues between μOR and δOR at this interface are likely not sufficient to prohibit an interaction at the TM5-TM6 interface.

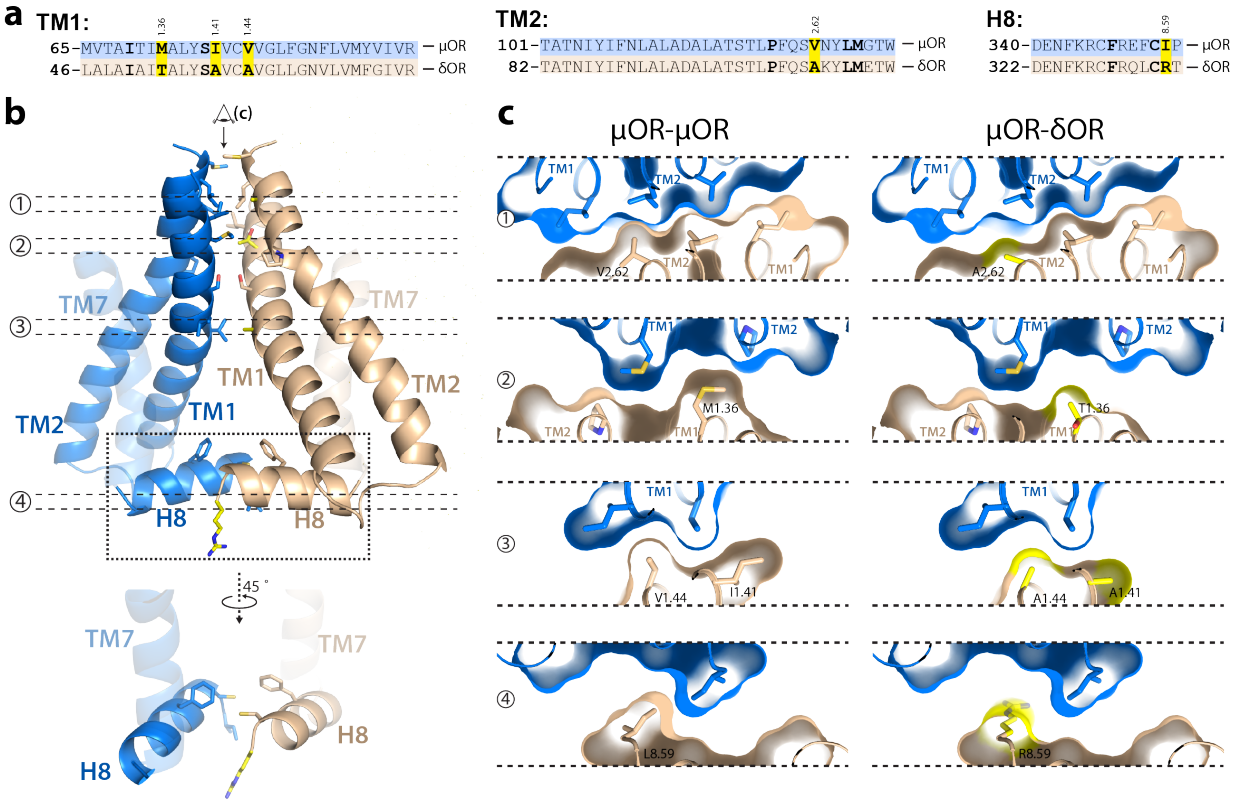

Supplementary Figure 10: Comparison of the TM1-TM2-H8 dimer interface between μOR-μOR and μOR-δOR.

While the primary intermolecular contact seen in the crystal structure of μOR occurs along TM5-TM6, an additional parallel contact is seen involving TMs 1-2 and Helix 8. **a,** Alignment of TM1, TM2 and Helix 8 sequences from the μOR and δOR. Interacting residues are shown in bold font, and non-strictly conserved residues are highlighted in yellow. **b**, Potential μOR-δOR four-helix bundle interface shown in detail with TM5-TM6 of μOR in blue and TM5-TM6 of δOR in beige. Yellow sticks indicate residues that are different in δOR as compared to μOR. Here, a homology model of δOR based on the μOR was aligned with the beige protomer. **c**, Tomographic representation along the dimer interface viewed from the extracellular side (as indicated in panel b). As for the TM5-TM6 interface, the differences between μOR and δOR result in a slightly different interaction network predicted for the TM1-TM2-H8 interface shown here.

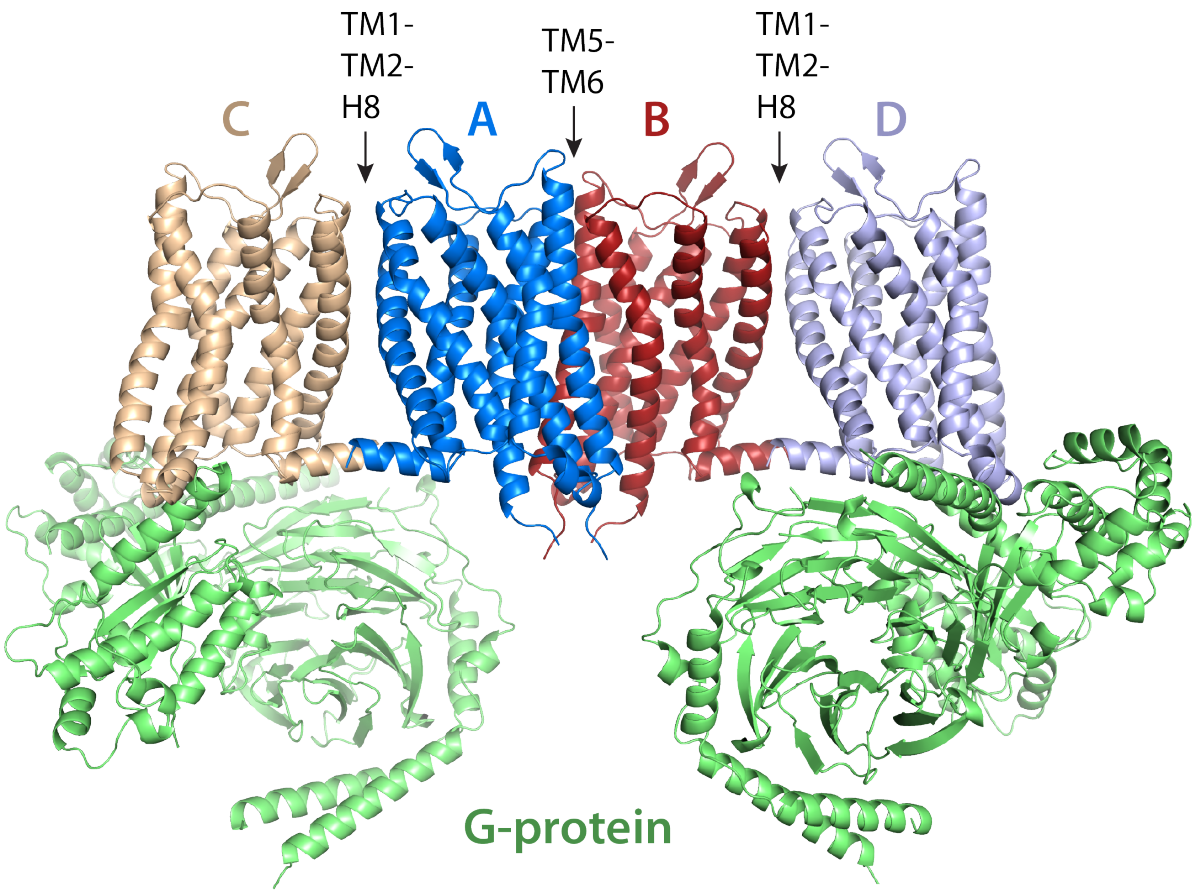

Supplementary Figure 11: Model for a μOR tetramer bound to G proteins.

This view shows a speculative molecular model of two active protomers (C and D), each bound to a G protein, which interact with two inactive protomers (A and B) via the TM1-TM2-Helix8 interface. In addition, inactive protomers A and B can interact via the TMs 5-6 interface without inducing steric clash between the G proteins. The active conformation of μOR (C and D) bound to the G protein was modeled from the crystal structure of the β_2-AR in complex with Gs[49].

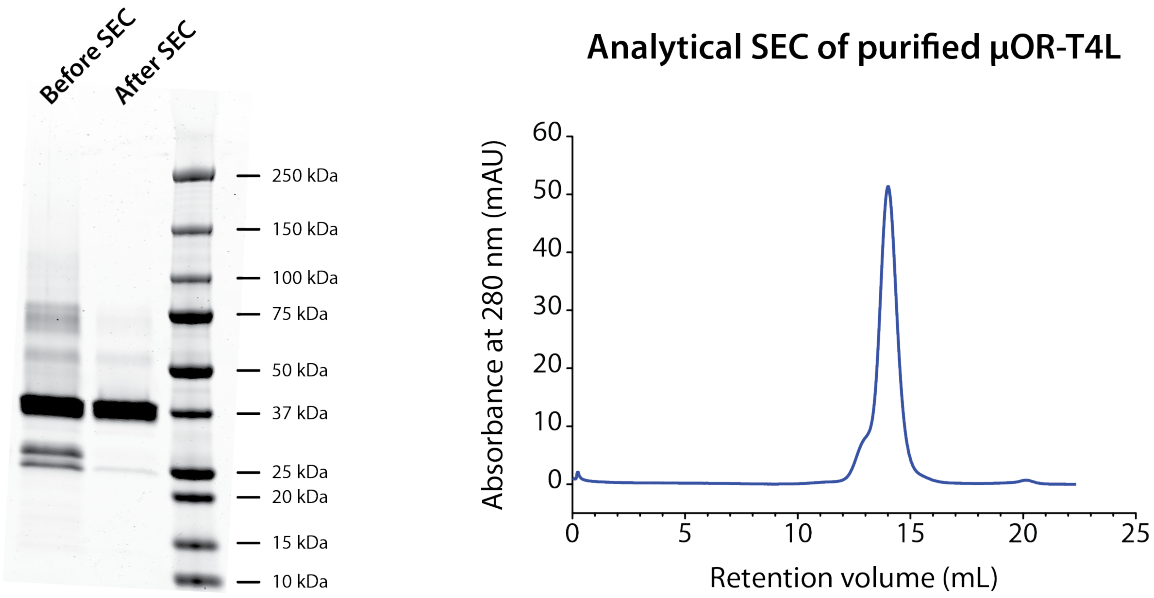

Supplementary Figure 12. SDS-PAGE and SEC of μOR-T4L used for crystallography.

SDS-PAGE before final size exclusion chromatography shows highly purified μOR-T4L with a small fraction of TEV and a small fraction of higher order oligomers and aggregates. Preparative size exclusion chromatography efficiently removes TEV and most higher order oligomers. An analytical size exclusion chromatogram (right) of the preparation used for crystallogenesis shows mostly monomeric μOR-T4L with a small portion of oligomeric μOR-T4L.

Supplementary table 1. Data collection and refinement statistics.

Data collection[a]	
Number of crystals	25
Space group	C2
Cell dimensions	
a, b, c (Å)	70.8, 174.7, 68.4
α, β, γ (°)	90, 107.8, 90
Resolution (Å)	30.5 – 2.8 (2.9 – 2.8)
R_{merge} (%)	14.4 (78.8)
$\langle I \rangle / \langle \sigma I \rangle$	10.6 (1.8)
Completeness (%)	99.0 (99.3)
Multiplicity	5.8 (5.5)
Refinement	
Resolution (Å)	30.5 – 2.8
No. unique reflections	18974 (946 in test set)
R_{work}/R_{free} (%)	23.3 / 27.5
Anisotropic *B* tensor (Å^2)	B_{11}= 23.2 / B_{22}= -18.4 / B_{33}= -4.8 / B_{12}= 0 / B_{13}= 9.0 / B_{23}= 0
Average *B*-factors (Å^2)	
μ opioid receptor	69.8
β–funaltrexamine	63.5
T4 lysozyme	91.7
Waters	58.3
Lipids	98.8
R.m.s. deviation from ideality	
Bond length (Å)	0.01
Bond angles (°)	0.93
Ramachandran statistics[b]	
Favored regions (%)	97.7
Allowed regions (%)	2.3
Outliers (%)	0

[a]Highest shell statistics are in parentheses. [b]As defined by MolProbity[50].

Bibliography

48 Chen, C. *et al.* Determination of the amino acid residue involved in [3H]beta-funaltrexamine covalent binding in the cloned rat mu-opioid receptor. *J. Biol. Chem.* **271**, 21422-21429 (1996).

49 Rasmussen, S. G. *et al*. Crystal structure of the beta2 adrenergic receptor-Gs protein complex. *Nature* **477**, 549-555 (2011).

50 Chen, V. B. *et al.* MolProbity: all-atom structure validation for macromolecular crystallography. *Acta. Crystallogr. D. Biol. Crystallogr.* **66**, 12-21 (2010).